Chern, dipole, and quadrupole topological phases of a simple magneto-optical photonic crystal with a square lattice and an unconventional unit cell

Zhihao Lan [1], Yafeng Chen [2,*], Liang An [2,†] and Zhongqing Su [2,‡]

[1] *Department of Electronic and Electrical Engineering, University College London, Torrington Place, London, WC1E 7JE, United Kingdom*

[2] *Department of Mechanical Engineering, The Hong Kong Polytechnic University, Kowloon, Hong Kong SAR 999077, China*

(Received 5 October 2023; revised 3 December 2023; accepted 13 December 2023; published 2 January 2024)

For the study of topological phases in photonics, while quantum-Hall-type first-order chiral edge states are routinely realized in magneto-optical photonic crystals, higher-order topological states are mostly explored in all-dielectric photonic crystals. In this work, we study both first- and second-order topological photonic states in magneto-optical photonic crystals. In specific, we revisit a simple magneto-optical photonic crystal in a square lattice with one gyromagnetic cylinder in each unit cell. However, rather than investigating the conventional unit cell where the cylinder is at the center of the square unit cell as previous works have done, we consider a configuration where the cylinders are located at the four corners of the square unit cell and show that this configuration hosts rich topological phases, such as dual-band Chern, dipole, and quadrupole topological phases. Our detailed characterizations of these topological states are based on the Wannier bands and their polarizations via the Wilson loop and nested Wilson loop methods. We study in detail both the edge and corner states of the different topological phases and show that they exhibit a special feature of "spectrum robustness." For example, though the edge and corner states of the dipole phases living in a band gap could be pushed into the bulk bands by tuning the boundary conditions, they can pass through the bulk bands and reappear within a different band gap. For dual-band quadrupole phases, we can find a regime where both band gaps host a set of corner states simultaneously and, intriguingly, the filling anomaly of one set of corner states can leave their signatures in the filling anomaly of the other set of corner states though they are separated by an extensive number of bulk states. The rich topological physics revealed in a simple magneto-optical photonic crystal not only provides new insights on higher-order topological phases in time-reversal symmetry-broken photonic systems, the results may also find promising applications by harnessing the potentials of both edge and corner states.

DOI: 10.1103/PhysRevB.109.045402

I. INTRODUCTION

Topological states in general could be classified as first order or higher order according to the codimension between those of the boundary state and its bulk. For example, if the boundary state lives in a dimension of one less than its bulk, it is a first-order topological state. On the other hand, if the difference between the dimensions of the boundary state and its bulk is larger than one, it is a higher-order topological state. In photonics, the first topological state proposed is the first-order quantum-Hall-type state introduced by Haldane and Raghu in 2008, where they constructed photonic analogs of chiral edge states from the quantum Hall effect originally discovered in two-dimensional (2D) electron gases under external magnetic fields [1,2]. A more practical implementation based on square-lattice gyromagnetic photonic crystals (PhCs) consisting of yttrium-iron-garnet (YIG) rods was proposed by Wang *et al.* [3] and the unidirectional backscattering-immune electromagnetic chiral edge states were later observed in microwave experiments [4]. After these seminal achievements, photonic quantum Hall states have been extensively investigated and many interesting phenomena and applications have been demonstrated to date, such as self-guiding unidirectional electromagnetic edge states without the ancillary cladding layer [5,6], multimode one-way waveguides with large Chern numbers [7,8], topological lasing in cavities of arbitrary geometries [9], photonic antichiral edge states [10,11], unpaired photonic Dirac point [12], nonlinear one-way frequency mixing [13], topological large-area waveguides [14,15], one-way bulk states [16], and chiral edge states in quasicrystals [17]. As magneto-optical effects in general are weak at optical frequencies, electromagnetic one-way edge states based on gyromagnetic materials and external magnetic fields to break the time-reversal symmetry are mostly limited to microwave frequencies. For detailed developments and applications of magneto-optical photonic crystals in topological physics, please see the recent review papers [18,19].

Higher-order topological phases were proposed recently by Benalcazar, Bernevig, and Hughes (BBH) [20,21] in an effort to quantize higher electric multipole moments in crystalline

*yachen@polyu.edu.hk
†liang.an@polyu.edu.hk
‡zhongqing.su@polyu.edu.hk

insulators, such as quadrupole and octupole moments. Such systems with quantized multipole moments exhibit gapped boundaries, which are themselves lower-dimensional topological phases. The BBH model for the topological quadrupole insulator is based on the tight-binding 2D Su-Schrieffer-Heeger (SSH) model with π-flux insertion [20,21], which requires both positive and negative hopping strengths between the nearest-neighbor lattice sites, and for photonic systems, this requirement is not easy to fulfill. Nonetheless, several platforms and methods for implementing the BBH π-flux model have been proposed and demonstrated, such as coupled ring resonators [22], plasmon-polaritonic nanocavities [23], and orbital-induced synthetic flux in waveguide arrays [24]. Moreover, other systems and techniques beyond the π-flux mechanism, such as twisted PhCs [25], magneto-optical PhCs [26,27], hexagonal and Lieb lattice PhCs [28–31], Floquet PhCs [32], and photonic Thue-Morse quasicrystals [33], have also been explored for photonic quadrupole topological phases. In general, for a bulk quadrupole moment to be well defined, the dipole moment of the bulk system has to vanish [21]. However, if one only concerns about corner states, it is not necessary to have a nontrivial bulk quadrupole moment. Instead, a nontrivial bulk dipole moment (i.e., bulk polarization) is also possible to result in corner states in systems with open edges and corners. This was theoretically demonstrated in 2D all-dielectric PhCs mimicking the SSH model with only positive hopping [34] and later confirmed in experiments with periodic dielectric rods on a perfect electric conductor (PEC) [35,36]. Additional developments of corner states based on nontrivial bulk dipole moments, such as dual-polarization corner states [37,38], multiband corner states [39,40], non-Hermitian corner states [41,42], etc., have been further pursued. Moreover, many interesting applications of corner states, such as high-quality-factor nanocavity [43,44], topological lasing [45,46], PhC fibers [47,48], rainbow trapping [49,50], nonlinear harmonic generation [51,52], topological edge and corner state coupling [53,54], and quantum information [55,56], have been demonstrated. For more details about higher-order topology and corner states, please see the recent review papers [57–59].

In this work, we revisit a simple magneto-optical PhC in a square lattice [3,4] and study both the first- and second-order topological phases of the system. Note that rather than focusing on the conventional unit cell where the gyromagnetic cylinder is at the center of the square unit cell, we consider a configuration where the cylinders are located at the four corners of the square unit cell [see Fig. 1(a)]. This configuration is motivated by a recent study [60], which shows that simply translating the conventional unit cell by half lattice constant along both x and y directions can result in nontrivial bulk polarizations. We find that this unconventional unit cell can lead to rich topological phases, such as quantum-Hall-type first-order topological phases (i.e., Chern phases) with the Chern number of $C = 1$, dual-band Chern phases with $C = -1$, dual-band second-order dipole phases with nontrivial bulk polarization of $p_x = p_y = \frac{1}{2}$, and dual-band second-order quadrupole phases with nontrivial bulk quadrupole moment of $q_{xy} = \frac{1}{2}$ [see Fig. 1(e)]. Our detailed characterizations of these topological phases are based on the Wannier bands and

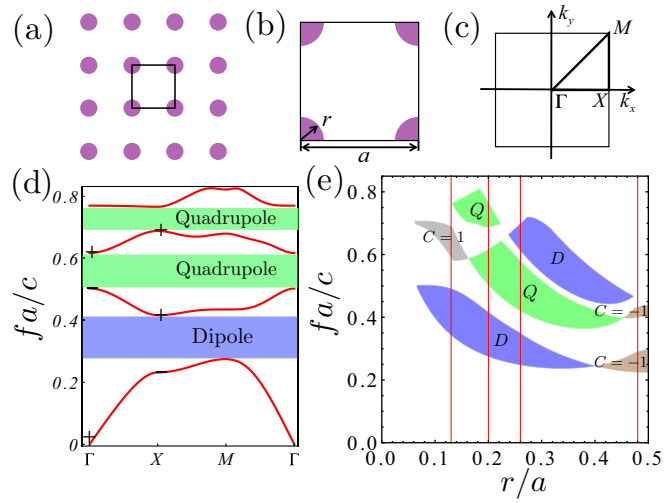

FIG. 1. (a) Schematic of a square-lattice magneto-optical PhC consisting of gyromagnetic cylinders in air. (b) Unit cell of the PhC as marked in (a) with lattice constant a and cylinder radius r. (c) First Brillouin zone of the PhC with the high-symmetry points Γ, X, and M marked. (d) Band structure of the PhC at $r = 0.2a$. Parameters of the gyromagnetic cylinders are $\epsilon = 15$, $\mu_0 = 1$, and $\mu_{21} = -\mu_{12} = 0.9i$. (e) Band-gap diagram as a function of r, where four typical band gaps at $r = 0.13$, $r = 0.2a$, $r = 0.26a$, and $r = 0.48a$ are marked by the red lines. D denotes dipole whereas Q quadrupole and $C = \pm 1$ is the Chern number of the band gap.

their polarizations via the Wilson loop and nested Wilson loop methods, which could provide a unified framework for calculating the Chern numbers, bulk dipole, and quadrupole moments of the bands.

We investigate both the edge and corner states of the different topological phases. In more detail, for the Chern phases, the nontrivial winding of the Wannier band determines the Chern number, leading to one-way edge states propagating along the system edges anticlockwise ($C = 1$) or clockwise ($C = -1$). For the dipole phases, though without nontrivial Wannier windings, the Wannier functions are located away from the center of the unit cell, corresponding to the obstructed atomic limit. The edge and corner states living in a band gap exhibit the feature of spectrum robustness, i.e., though the edge and corner states could be pushed into the bulk bands by tuning the boundary conditions, they can pass through the bulk bands and reappear within a different band gap. For the quadrupole phases, though the whole system has vanishing bulk dipole moment, the polarization of the Wannier band itself could lead to nontrivial bulk quadrupole moment. We can realize a dual-band regime where both band gaps host a different set of corner states and, intriguingly, the filling anomaly of one set of corner states can leave their signatures in the filling anomaly of the other set of corner states though they are separated by an extensive number of bulk states. This is a different manifestation of the spectrum robustness of the corner states. The rich topological physics revealed in a simple magneto-optical PhC not only sheds new light on higher-order topological phases in time-reversal symmetry-broken systems, the results may also offer new opportunities

for practical applications by harnessing the merits of both edge and corner states.

The paper is organized as follows. In Sec. II, we present the model system and its main phase diagram. In Sec. III, we describe the computational method based on the tools of Wilson loop and nested Wilson loop for characterizing topological properties of the system. In Sec. IV, we discuss the Chern phases, their Wannier band windings, and chiral edge states. In Sec. V, we show the dipole phases, their edge and corner states. In Sec. VI, we study the quadrupole phases, edge-localized polarizations, corner states, and filling anomaly. We conclude and discuss some future directions in Sec. VII.

II. MODEL SYSTEM AND ITS TOPOLOGICAL PHASES

The model system we consider in this work is a simple 2D magneto-optical PhC consisting of gyromagnetic cylinders with radius r, which are embedded in air and arranged in the square lattice with lattice constant a [see Fig. 1(a)]. The permeability tensor of the gyromagnetic cylinders acquires off-diagonal terms under an external magnetic field perpendicular to the 2D PhC and, for simplicity of the discussions, we keep $\mu_0 = 1$ and add the off-diagonal terms μ_{21} and μ_{12} to account for the magnetic field and time-reversal symmetry-breaking effects. Note also that different from the conventional unit cell as studied previously [3,4,7,8], where the cylinder is at the center of the unit cell, in this work we consider an unconventional unit cell, where the cylinders are located at the four corners of the square unit cell [see Fig. 1(b)] as recent works have demonstrated that this configuration could naturally have nontrivial bulk polarizations [34,60]. Figure 1(c) shows the first Brillouin zone of the PhC in momentum space, where the high-symmetry points Γ, X, and M are marked. Moreover, we will only focus on the transverse magnetic (TM) modes of the PhC in this work, which have nonzero components of E_z, H_x, and H_y.

A typical band diagram for the TM modes of the PhC with cylinder radius $r = 0.2a$ is shown in Fig. 1(d), where the first three band gaps show dipole and quadrupole topological properties. We only consider the first three lowest band gaps in this work, as they already host all the interesting topological phases we would like to illustrate. Meanwhile, the lower-order band gaps usually have relatively large sizes and thus the bulk-edge-corner correspondence could be more easily manifested in the study of edge and corner states. Note that though the band diagram of the PhC does not depend on the choice of the unit cell, the topological properties of the bands and band gaps can be different for different kinds of unit cell. The parities of the eigenmodes at high-symmetry points Γ and X are also marked in the band diagram as "$\pm$," which could be used conveniently to derive the topological properties of the band gaps [60,61].

In specific, if the parities of a band at Γ and X have different sign, i.e., a parity inversion happens, then this band for a C_4-symmetric PhC has a nontrivial bulk polarization of $p_x = p_y = \frac{1}{2}$ (defined only to modular 1). According to this criterion, the first and second bands have nontrivial polarizations whereas the third band has a zero polarization and, consequently, the polarizations of the first, second, and third band gaps (i.e., the sum of polarizations of all the bands below the band gap) show nontrivial, trivial, and trivial features, respectively. On the other hand, the quadrupole moment of a band could be defined as $q_{xy} = p_x p_y$ and the quadrupole moment of a band gap (defined only to modular 1) is simply the sum of all the quadrupole moments of the bands below the band gap [28]. Note also that for the quadrupole moment of a band gap to be well defined, the dipole moment of it has to vanish [21]. According to these criteria, the first and second bands have $q_{xy} = \frac{1}{4}$ whereas the third band has $q_{xy} = 0$ and, consequently, one can deduce that the second and third band gaps host a nontrivial quadrupole moment of $q_{xy} = \frac{1}{2}$. In the following, more sophisticated methods based on the Wannier bands and their polarizations via the Wilson loop and nested Wilson loop techniques will be used to confirm the dipole and quadrupole moments derived above based on the symmetry properties of the parities at Γ and X.

The evolution of the topological nature of the band gaps as a function of the cylinder radius r is presented in Fig. 1(e), which show Chern, dipole, and quadrupole topologically phases. Interestingly, this simple PhC structure with an unconventional unit cell can host dual-band Chern, dipole, and quadrupole phases at $r = 0.48a$, $0.26a$, and $0.2a$, respectively. It can also have two different Chern phases with $C = +1$ at $r = 0.13a$ and $C = -1$ at $r = 0.48a$. These four cases as marked by the red lines in Fig. 1(e) will be discussed in detail in the following sections.

III. COMPUTATIONAL METHOD BASED ON THE WILSON LOOP TECHNIQUE

In this section, we briefly outline the computational method for characterizing the topological properties of crystalline insulators based on the Wilson loop and nested Wilson loop techniques originally developed by Benalcazar *et al.* [21]. To use this method in the context of photonics [62–64], one would need to first obtain the eigenmodes u_k^n of the PhC using any available eigensolver (e.g., COMSOL). For the TM modes of the PhC we consider in this work, the key quantity needed for such computation is the field profile of $E_z^n(k)$, i.e., the spatially periodic part of the Bloch function for the nth band. Based on the eigenmodes u_k^n [we denote $u_k^n \equiv E_z^n(k)$ in the following], one can define the Wilson line element from $k = (k_x, k_y)$ to $k + \Delta_x$ along the x direction as

$$F_{k,\Delta_x}^{mn} = \iint_{\text{unit cell}} dx\, dy\, u_{k+\Delta_x}^{m*}(x,y)\epsilon(x,y)u_k^n(x,y), \qquad (1)$$

where $\epsilon(x, y)$ is the dielectric distribution and the integral is done within the unit cell. From the Wilson line element, one can construct a Wilson loop winding along the x direction and crossing the whole first Brillouin zone (i.e., $k \to k + 2\pi\hat{x}$) as

$$W_{k,x} \equiv F_{k+2\pi\hat{x}-\Delta_x,\Delta_x} \ldots F_{k+\Delta_x,\Delta_x} F_{k,\Delta_x}. \qquad (2)$$

Note that due to the periodic boundary conditions of the square first Brillouin zone, the above result implies a closed loop in the Brillouin torus [see Fig. 2(a)]. The Wilson loop is a $N_{\text{occ}} \times N_{\text{occ}}$ matrix with N_{occ} the number of bands below the band gap of interest. Then one can diagonalize the Wilson

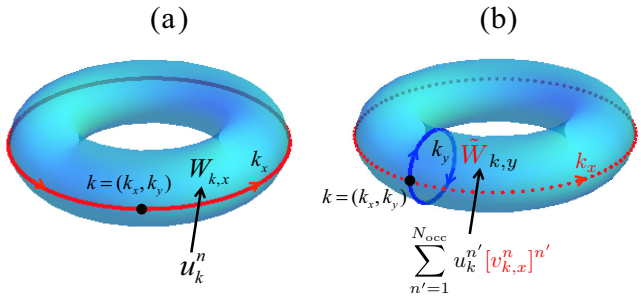

FIG. 2. Illustration of the Wilson loop (a) and nested Wilson loop (b) methods using the Brillouin torus. In the Wilson loop method (a), the Wilson loop matrix $W_{k,x}$ starting from a base point $k=(k_x,k_y)$ and winding along x is constructed from the eigenmodes $u_k^n(x,y)$ of the PhC. In the nested Wilson loop method (b), the Wilson loop matrix $\tilde{W}_{k,y}$ starting from a base point $k=(k_x,k_y)$ and winding along y is constructed from the hybrid eigenmodes $\sum_{n'=1}^{N_{occ}} u_k^{n'}[v_{k,x}^n]^{n'}$, where $[v_{k,x}^n]^{n'}$ is the n'th component of the nth Wilson loop eigenstate $v_{k,x}^n$ obtained from the Wilson loop matrix $W_{k,x}$ winding along x.

loop matrix as

$$W_{k,x}\left|v_{k,x}^j\right\rangle = e^{i2\pi v_x^j(k_y)}\left|v_{k,x}^j\right\rangle. \tag{3}$$

The phases $v_x^j(k_y)$ with $j=1\ldots N_{occ}$ are the Wannier centers, which correspond to the average positions of the electromagnetic wave functions relative to the center of the unit cell. Note that as $v_x^j(k_y)$ has a dependence on k_y, the Wannier centers in general form bands, i.e., Wannier bands. The k_y-resolved polarization $p_x(k_y)$ along the x direction can be obtained by summing over all the Wannier bands below the band gap as $p_x(k_y)=\sum_{j=1}^{N_{occ}} v_x^j(k_y)$. Finally, the total polarization of the system along x could be obtained by integrating over the momentum k_y, i.e., $p_x=\frac{1}{2\pi}\int_0^{2\pi} dk_y p_x(k_y)$. The polarization p_y along the y direction could be analyzed similarly, however, due to the C_4 symmetry of the PhC we consider in this work, one can simply get $p_y=p_x$ by symmetry and thus it suffices to consider only the results along x.

For the three topological phases we will be focusing on in this work, i.e., the Chern, dipole, and quadrupole phases, the topological invariants for characterizing these phases could be calculated conveniently via the above framework based on Wannier bands. First, for the Chern phases, the winding behavior of the Wannier band determines the Chern number. To show this, we note that the Chern number is defined to be

$$C=\frac{1}{2\pi}\int_{\mathrm{BZ}} d^2k\,\mathrm{Tr}[F(k)], \tag{4}$$

where $F(k)=\partial_{k_x}A_{y,k}-\partial_{k_y}A_{x,k}$ is the Berry curvature and $A_{i,k}^{mn}=-i\langle u_k^m|\partial_{k_i}|u_k^n\rangle$ with $i=x,y$ is the Berry connection. Choosing the gauge $\partial_{k_x}A_{y,k}=0$ [21], one can obtain

$$\begin{aligned} C&=\frac{1}{2\pi}\int_{\mathrm{BZ}} d^2k(-\partial_{k_y}\mathrm{Tr}[A_{x,k}])\\ &=\int_0^{2\pi} dk_y\partial_{k_y}\left(-\frac{1}{2\pi}\int_0^{2\pi} dk_x\mathrm{Tr}[A_{x,k}]\right)\\ &=\int_0^{2\pi} dk_y\partial_{k_y}p_x(k_y). \end{aligned} \tag{5}$$

The above result implies that the Chern number C could be determined by the winding of the Wannier band $p_x(k_y)$, whose winding direction gives the sign of the Chern number whereas the number of times of winding over the momentum k_y gives the absolute size of the Chern number. Note that, if one uses $p_y(k_x)$ for the winding calculations, the sign obtained would be opposite compared to that obtained from $p_x(k_y)$. The Chern number could also be calculated from Eq. (4) by discretizing the first Brillouin zone and performing the numerical integral of the Berry curvature [65,66]. Typically, Chern phases in photonic systems are created in magneto-optical PhCs, where the time-reversal symmetry is broken by external magnetic fields.

For the dipole phases, they are characterized by the polarization $p=(p_x,p_y)$ and are mostly studied in systems preserving the time-reversal symmetry, e.g., all-dielectric materials. The Wannier band $p_x(k_y)$ typically locates around $p_x=0$ or $p_x=\pm 0.5$, showing trivial or nontrivial polarization. A primary requirement for the quadrupole moment to be well defined is that the polarization has to vanish because a bulk quadrupole moment is only well defined with zero bulk dipole moment. To characterize the quadrupole phases, one would need the nested Wilson loop method as the Wannier sector $v_x(k_y)$ itself may also have nontrivial polarization along y. To use the nested Wilson loop method, one would need to first construct a new basis $\tilde{u}_{k,x}^j$ through $\tilde{u}_{k,x}^j=\sum_{n=1}^{N_{occ}} u_k^n[v_{k,x}^j]^n$, where $[v_{k,x}^j]^n$ is the nth component of the jth Wilson loop eigenstate $|v_{k,x}^j\rangle$ obtained from $W_{k,x}$. With this new basis, we can repeat the Wilson loop calculation defined above but with winding along the y direction in order to resolve the polarization of the Wannier sector $v_x(k_y)$ [see Fig. 2(b) for illustration]. Writing this new nested Wilson loop as $\tilde{W}_{k,y}^{v_x}$, we can diagonalize it as

$$\tilde{W}_{k,y}^{v_x}\left|v_{k,y}^{v_x,j}\right\rangle = e^{i2\pi v_y^{v_x,j}(k_x)}\left|v_{k,y}^{v_x,j}\right\rangle, \tag{6}$$

where $v_y^{v_x,j}(k_x)$ is the polarization of the Wannier sector $v_x^j(k_y)$. Similarly, one can define the k_x-resolved total polarization $p_y^{v_x}(k_x)$ over the Wannier sector v_x by summing over all the occupied bands and then obtain the total polarization $p_y^{v_x}$ of the system by integrating over k_x. The meaning of the Wannier sector polarization is as follows: the existence of a Wannier gap along x implies a spatial separation of the electromagnetic wave function along x. Then a nonzero polarization in the y direction of such a Wannier sector implies a shift of that sector up and down along y, thus offering the possibility to form a nontrivial bulk quadrupole moment defined by

$$q_{xy}=\sum_{j=1}^{N_{occ}} p_y^{v_x^j} p_x^{v_y^j}. \tag{7}$$

Finally, the Wilson loop method could also be applied to a supercell that is periodic along x and has finite unit cells (N_y) along y, which can be simply viewed as a one-dimensional (1D) periodic system along x. In this case, it is convenient to define the unit cell R_y ($R_y=1\ldots N_y$) resolved polarization

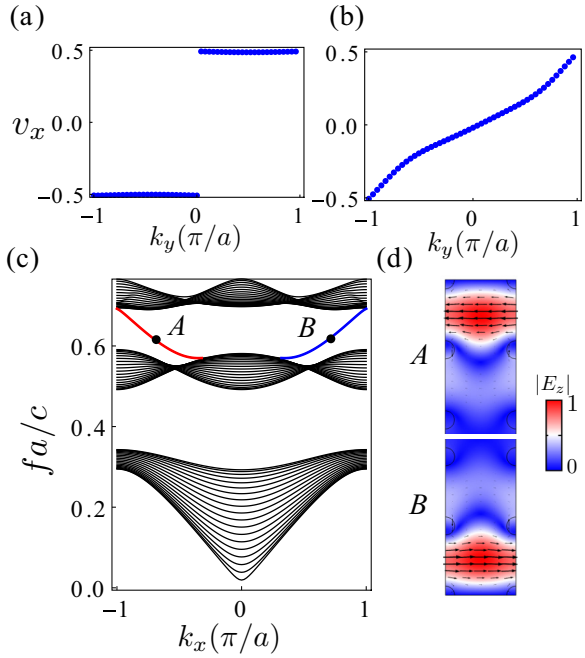

FIG. 3. Photonic Chern phase at $r = 0.13a$. (a) Wannier band for the first energy band, which shows nontrivial polarization around $p_x = \pm 0.5$. (b) Wannier band for the second energy band, which shows positive winding as a function of k_y, giving a Chern number of $C = +1$. (c) Projected band diagram of a supercell with 20 unit cells along y (with PEC boundary conditions) and periodic along x. The red and blue curves correspond to the chiral edge states located at the top and bottom edges of the supercell, propagating leftward and rightward, respectively. (d) Field profile and Poynting vector distributions for the two eigenmodes marked as A and B in (c).

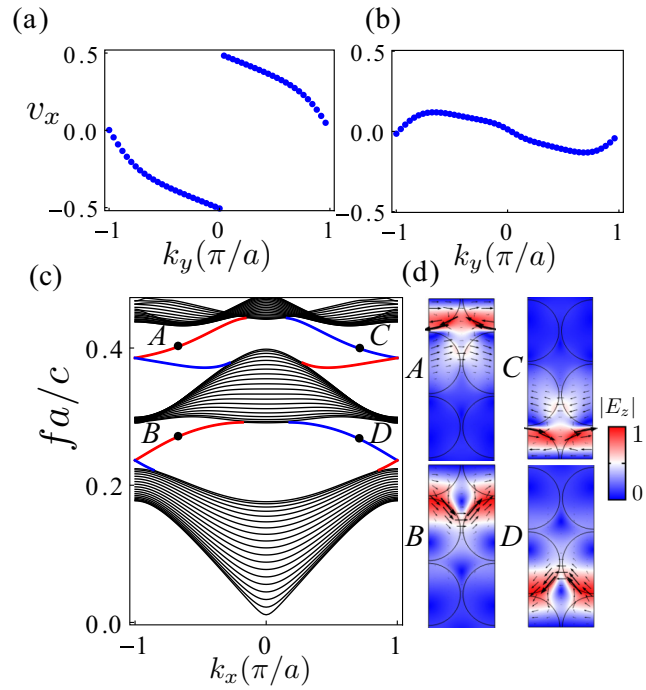

FIG. 4. Photonic Chern phase at $r = 0.48a$. (a) Wannier band for the first energy band, which shows negative winding as a function of k_y, giving a Chern number of $C = -1$. (b) Wannier band for the second energy band, which shows trivial polarization around $p_x = 0$. (c) Projected band diagram of a supercell with 20 unit cells along y (with PEC boundary conditions) and periodic along x. The red and blue curves correspond to the chiral edge states located at the top and bottom edges of the supercell, propagating rightward and leftward, respectively. (d) Field profile and Poynting vector distributions for the four eigenmodes marked as A, B, C, and D in (c).

along the y direction via

$$p_x(R_y) = \sum_{j=1}^{N_{\text{occ}}} \rho^j(R_y) v_x^j \tag{8}$$

with $\rho^j(R_y) = \int_0^a dx \int_{(R_y-1)a}^{R_y a} dy \sum_{k_x} \tilde{u}^{j*}_{k_x,x}(x,y)\epsilon(x,y)\tilde{u}^{j}_{k_x,x}(x,y)$, where $\tilde{u}^{j}_{k_x,x}(x,y)$ is the hybrid basis defined above. This unit-cell resolved polarization is convenient to show the emergence of edge-localized polarization due to nontrivial bulk topology.

IV. PHOTONIC CHERN PHASES

We first discuss the Chern phases of the system. Our simple PhC can have two kinds of Chern phases, one with $C = +1$ at small r and one with $C = -1$ at large r. At $r = 0.13a$ as shown in Fig. 1(e), the first band gap is a dipole band gap with nontrivial bulk polarization whereas the second band gap is a Chern phase with Chern number of $C = +1$. The Wannier bands $v_x(k_y)$ for the first two energy bands calculated using the Wilson loop method are shown in Figs. 3(a) and 3(b). Figure 3(a) shows that the first band has a nontrivial polarization of $p_x = 0.5$ without winding (note that the polarization is defined only up to modular 1). Figure 3(b) shows that the second band has a nontrivial winding as a function of k_y, giving a Chern number of $C = +1$. To show that there will be chiral edge states emerging within the second band gap due to the nontrivial gap Chern number of $C = +1$, we consider a supercell of 20 unit cells along y (with PEC boundary conditions at the two open ends) while periodic along x. The projected band diagram of the supercell is shown in Fig. 3(c), from which one can see the emergence of one-way edge states within the band gap, where the red colored curve corresponds to the one-way edge states located at the top edge whereas the blue colored curve corresponds to these located at the bottom edge. The field profiles ($|E_z|$) of the two eigenmodes marked as A and B in Fig. 3(c) are presented in Fig. 3(d), from which one can see that they are indeed localized at the top and bottom edges. Moreover, from the Poynting vector distributions, one can see that the eigenmode A at the top edge propagates to the left whereas the eigenmode B at the bottom edge propagates to the right, which are consistent with their group velocities, i.e., the slope of the edge-state dispersion curve.

For the Chern phase at $r = 0.48a$, the Wannier bands of the first two energy bands are shown in Figs. 4(a) and 4(b). Figure 4(a) shows that the first band has a nontrivial winding opposite to that of Fig. 3(b), thus resulting in a negative Chern number of $C = -1$. Meanwhile, the second band has a trivial polarization of $p_x = 0$ without winding. As the gap Chern number is the sum of the Chern numbers of all the bands below the band gap, this means that both the first and

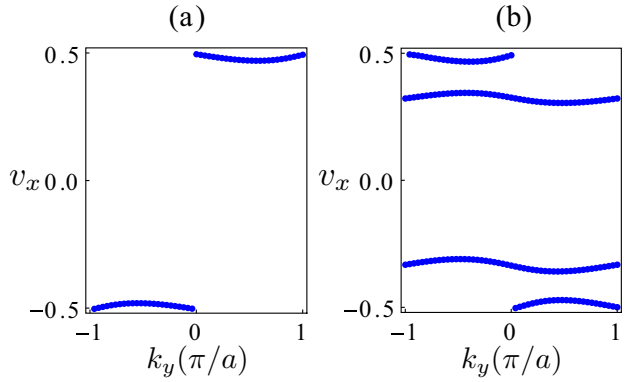

FIG. 5. Wannier bands $v_x(k_y)$ for the first (a) and third (b) band gaps at $r = 0.26a$, which show nontrivial polarization of $p_x = 0.5$ for both band gaps.

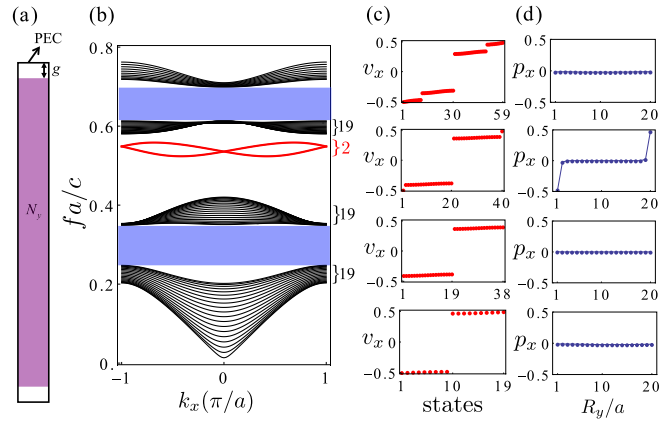

FIG. 6. Edge states and edge-localized polarizations at $r = 0.26a$. (a) Supercell with N_y unit cells along the y direction and periodic along the x direction. PEC boundary conditions are applied at the two open ends along y with an air gap of size g. (b) Projected band diagram of the supercell with $N_y = 20$ and $g = 0$, where the number of states for the bulk and edge bands are marked to show the topological feature of the system. The two dipole bandgap are shaded as light blue. (c) Wannier centers of the bands at different fillings of $f = 19$, 38, 40, and 59. (d) Unit-cell (R_y) resolved polarization along y at different fillings corresponding to (c).

second band gaps have a gap Chern number of $C = -1$, i.e., there will be chiral edge states emerging both in the first and second band gaps. To demonstrate this, a similar supercell as in Fig. 3 is considered and its projected band diagram is shown in Fig. 4(c), from which one can see that chiral edge states indeed emerge within both the first and second band gaps. The field profiles of four eigenmodes marked as A, B, C, and D in Fig. 4(c) are presented in Fig. 4(d), from which one can see that while the eigenmodes A and B are localized at the top edge of the supercell, the eigenmodes C and D are localized at the bottom edge. Moreover, from the Poynting vector distributions, one can see that while eigenmodes A and B move to the right, eigenmodes C and D move to the left, also consistent with the slope of the edge-state dispersion curve. It is to be noted that the edge states in Fig. 3(c) and those of Fig. 4(c) at the same edge counterpropagate with each other, due to their opposite Chern numbers.

V. PHOTONIC DIPOLE PHASES

In this section we study the double dipole band gaps at $r = 0.26a$ [see Fig. 1(e)], where the first and third band gaps show nontrivial bulk polarizations. The Wannier bands for all the energy bands below the first and third band gaps are shown in Figs. 5(a) and 5(b), respectively. From Fig. 5(a), we can see that the Wannier band for the first band gap locates around ± 0.5 and thus has a nontrivial polarization of $p_x = 0.5$ after integration over k_y. For the third band gap, which contains three Wannier bands, the two bands close to $v_x = 0$ cancel with each other and thus the total polarization is also nontrivial of $p_x = 0.5$. The nontrivial bulk polarizations will result in edge and corner states in systems with open edges and corners.

Before studying the edge states of the dipole phases, we would like to clarify a main difference between the Chern phases and the dipole and quadrupole phases. In general, all topological phases are related to some topological invariants. While the bulk topological invariant only provides a basis for the existence of topological edge states, details of the edge states, such as shape of their dispersion curve and/or location of the states in the spectrum, are related to the specifics of the boundary conditions. The Chern number has its root from the nontrivial distribution of the Berry curvature in the whole Brillouin zone whereas the dipole and quadrupole moments could be determined by the symmetry indicators at certain local points of the Brillouin zone. As such, the topology of the Chern phases is more strong than that of the dipole and quadrupole phases in the sense that the resulting topological edge states of the Chern phases are gapless, i.e., they cross the whole band gap and are connected with the bulk states both up and below the band gap [see Figs. 3(c) and 4(c)] and thus can not be removed outside of the band gap as long as the band gap persists (though the shape of their dispersion curve can still be tailored by the boundary conditions [13]). On the other hand, the topological edge states of the dipole and quadrupole phases in general are gapped, which lack the necessary mechanism to pin their position within the corresponding band gap, i.e., their location in the spectrum strongly depends on the boundary conditions and is not constrained by the topological invariants of dipole or quadrupole moments themselves.

To study the topological edge states of the dipole phases, we consider a supercell consisting of N_y unit cells along the y direction whereas periodic along x. Furthermore, to understand the effect of the boundary conditions on the spectrum of the edge states, we consider PEC boundary conditions at the two open ends and introduce an air gap of size g between the supercell and the PEC [see Fig. 6(a)]. The projected band diagram of the supercell at $N_y = 20$ and $g = 0$ is shown in Fig. 6(b), from which one can see the emergence of edge states in the spectrum. Unexpectedly, the emergent edge states are not located within the first and third dipole band gaps but are within the second quadrupole band gap. To understand this unusual behavior, we label the number of bulk and edge states in the spectrum [see the right of Fig. 6(b)]. As there are $N_y = 20$ unit cells along the y direction, for a system without any topology, the number of states for each bulk band should

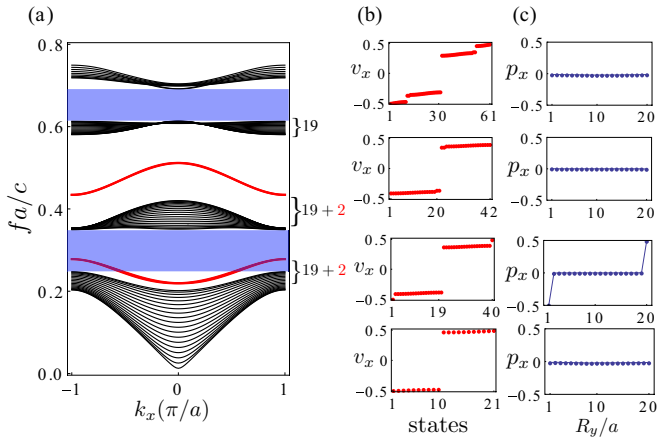

FIG. 7. (a) Projected band diagram of the supercell in Fig. 6(a) with $N_y = 20$ and $g = 0.5a$ at $r = 0.26a$, where the number of states for the bulk and edge bands are marked to show the topological feature of the system. The two dipole band gaps are shaded as light blue. (b) Wannier centers of the bands at different fillings of $f = 21, 40, 42$, and 61. (c) Unit-cell (R_y) resolved polarization along y at different fillings corresponding to (b).

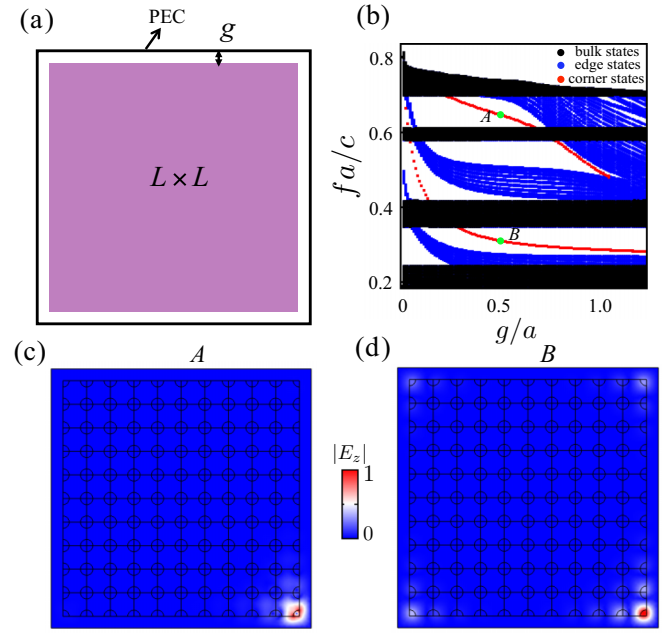

FIG. 8. Corner states of the two dipole band gaps at $r = 0.26a$. (a) Schematic of a finite PhC with size of $L \times L$ unit cells, where PEC boundary conditions with an air gap of size g between the PEC and the PhC are used. (b) Spectrum of the finite PhC in (a) with $L = 10$ as a function of g, where two sets of corner states A and B at $g = 0.5a$ are marked. The bulk, edge, and corner states are colored as black, blue, and red, respectively. (c), (d) The field profile ($|E_z|$) of one representative corner state from the set A and B, respectively.

be exactly 20. However, we could see that there are only 19 states for each of the three bulk bands, which means that these bands have nontrivial topology and thus lead to the counting mismatch [61]. We further show in Fig. 6(c) the Wannier centers of the states at different fillings of $f = 19, 38, 40$, and 59. From the results, one can see that when the filling covers the two edge states, there are two additional states appearing at 1 and 40 in the Wannier center spectrum. The unit-cell resolved polarizations are shown in Fig. 6(d), from which one can see that apart from the edge-localized polarization when the two edge states are filled, all the other cases have no edge polarization. For the edge-localized polarizations, their values at the two ends of $R_y = 1$ and 20 have different signs with $p_x = -0.5$ and $+0.5$, respectively.

To understand the effect of the air gap size g on the location of the edge states in the spectrum, we show in Fig. 7(a) the projected band diagram similar to Fig. 6(b) but with $g = 0.5a$. The results show that the two edge states in the second quadrupole band gap of Fig. 6(b) are brought down to the first dipole band gap whereas additional states from the fourth bulk band are brought down to the second quadrupole band gap [see Fig. 8(b)]. In general, we could expect that when the size of the air gap g increases, the frequency of the edge states will decrease due to the loosened confinement for the edge states around the air gap. To study the polarization behaviors at different fillings, we show in Fig. 7(b) the Wannier centers of the states at fillings of $f = 21, 40, 42$, and 61. The corresponding edge-localized polarizations are shown in Fig. 7(c). Interestingly, from the results in Figs. 7(b) and 7(c), one can see that only when the filling is at $f = 40$, i.e., below the edge states within the second band gap, the system shows edge-localized polarization. This is different from the filling at $f = 21$, where even though the filling also covers the two edge states, there is no edge-localized polarization at the system edges.

The dipole band gaps can also induce corner states. However, different from previous works, where two trivial and nontrivial PhCs are used to construct four corners, here we only consider a finite PhC consisting of $L \times L$ unit cells as shown in Fig. 8(a) with PEC boundary conditions. Again, to study the effect of the PEC boundaries on the location of the corner states in the spectrum, we introduce a small air gap between the PEC and the finite PhC [see Fig. 8(a)]. The spectrum of the finite system in Fig. 8(a) as a function of the air gap size g is shown in Fig. 8(b), where the bulk, edge, and corner states are colored as black, blue, and red, respectively. To demonstrate that the states marked by A and B in Fig. 8(b) are indeed corner states, we show in Figs. 8(c) and 8(d) the field profiles of two representative corner states for A and B, from which one can see that their fields are indeed localized around the system corners, indicating their nature as corner states.

In general, the size of the air gap will have negligible effect on the frequency of the bulk states because the weight of the field profiles of the bulk states within the air gap is small. Differently, with their field distributions mostly located around the air gap, the frequencies of the edge and corner states will be strongly affected by the size of the air gap. One can expect that with the increasing of the size of the air gap, the frequencies of the edge and corner states will decrease as the confinement effect of the air gap is weakened. It is interesting to see that by changing the size of the air gap, the location of the corner states in the spectrum could be continuously tuned. For example, as shown in Fig. 8(b),

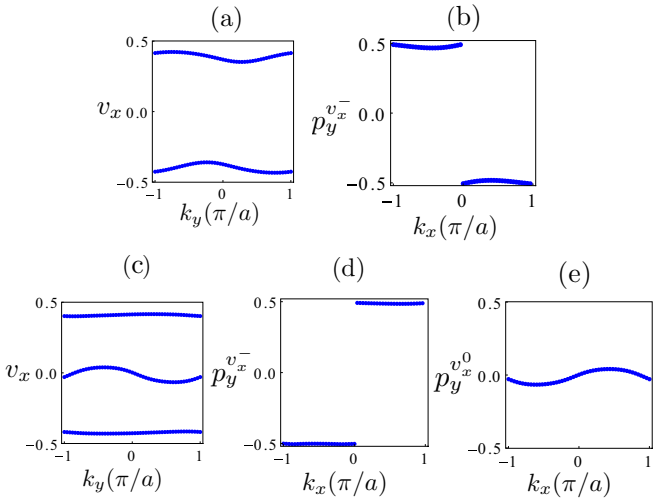

FIG. 9. Wannier bands $v_x(k_y)$ and their polarizations $p_y^{v_x}(k_x)$ for the second (a), (b) and third (c)–(e) quadrupole band gaps at $r = 0.2a$. In (b) only the polarization for the lowest band (v_x^-) is shown whereas in (d) and (e) the polarizations for the lowest band (v_x^-) and zero-polarization band (v_x^0) are shown. The polarization for v_x^+ is not shown due to the symmetry between $p_y^{v_x^+}$ and $p_y^{v_x^-}$.

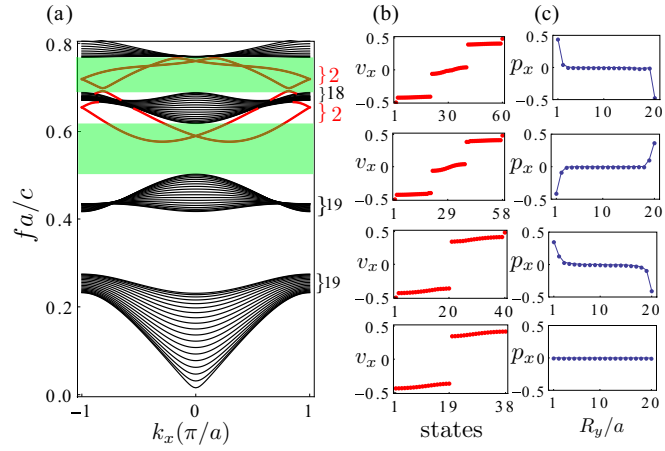

FIG. 10. (a) Projected band diagram of the supercell in Fig. 6(a) with $N_y = 20$ and $g = 0$ at $r = 0.2a$, where the numbers of states for the bulk and edge bands are marked to show the topological properties of the system. The two quadrupole band gaps are shaded as light green. (b) Wannier centers of the bands at different fillings of $f = 38, 40, 58$, and 60. (c) Unit-cell resolved polarization along y at different fillings corresponding to (b).

when the size of the air gap decreases from $g = 1.0a$ to zero, the corner states of the B branch in the first dipole band gap could be pushed to the second band gap and then to the third band gap and similarly for the corner states of the A branch. This demonstrates a special feature of the corner states, i.e., their spectrum robustness, which means that even though they could be pushed to and imbedded within the bulk states, they can cross the bulk states and reappear within a different band gap, highlighting the topological nature of these states. The edge states exhibit a similar feature, i.e., they can cross the bulk states and reappear within a different band gap when changing the size of the air gap since they are also originated from the nontrivial topology of bulk polarization.

VI. PHOTONIC QUADRUPOLE PHASES

In this section, we study the double quadrupole band gaps at $r = 0.2a$ [see Fig. 1(e)]. The Wannier bands for the energy bands below the second and third band gaps are shown in Figs. 9(a) and 9(c), respectively. For the Wannier bands of the second band gap, we can see that the total polarization is zero. The polarization of the lower Wannier sector is shown in Fig. 9(b), which exhibits a nontrivial polarization of $p_y^{v_x^-} = \frac{1}{2}$. Note that the polarization of the higher sector $p_y^{v_x^+} = \frac{1}{2}$ due to the symmetry. The polarizations of other sectors can be deduced by symmetry and as such the total quadrupole moment for this band gap is $q_{xy} = p_y^{v_x^-} p_x^{v_y^-} + p_y^{v_x^+} p_x^{v_y^+} = \frac{1}{2}$. Similarly, for the Wannier bands of the third band gap shown in Fig. 9(c), one can see that the total polarization of the three bands is also zero and in Figs. 9(d) and 9(e), we present the polarizations of the lower ($p_y^{v_x^-}$) and middle ($p_y^{v_x^0}$) Wannier sectors. While the lower sector shows a nontrivial polarization, the middle sector has a zero polarization and as such, the total quadrupole moment of the third band gap is also $\frac{1}{2}$, i.e., $q_{xy} = p_y^{v_x^-} p_x^{v_y^-} + p_y^{v_x^0} p_x^{v_y^0} + p_y^{v_x^+} p_x^{v_y^+} = \frac{1}{2}$. So these results of the Wannier bands and their polarizations confirm that our system hosts dual-band quadrupole topological phases, which have not been reported previously in photonic systems.

The nontrivial bulk quadrupole moment will lead to edge and corner states in systems with open edges. To study the edge states, we calculate the spectrum of a supercell as shown in Fig. 6(a) with $N_y = 20$ and $g = 0$ and present the results in Fig. 10(a). To illustrate the topological properties of the bands, we label the number of states for the bulk and edge bands [see the right of Fig. 10(a)]. It is interesting to see that, different from the dipole cases, there are edge states emerging within the second and third quadrupole band gaps. Meanwhile, one can see that the first and second bulk bands have a counting mismatch of 1 band due to their nontrivial polarizations whereas the third bulk band has a counting mismatch of 2 bands due to its trivial polarization [see the result of parity inversion for the three bulk bands in Fig. 1(d)]. The Wannier centers of the states at different fillings of $f = 38, 40, 58, 60$ are shown in Fig. 10(b). One can see that when the filling covers the edge states, there are edge localized polarizations appearing at $v_x = \pm 0.5$. The unit-cell resolved polarizations are shown in Fig. 10(c), from which one can see that at fillings of $f = 40, 58, 60$, nontrivial polarizations appear at the two ends $R_y = 0$ and $20a$ of the supercell.

Next, we increase the air gap between the PEC boundaries and the PhC supercell to study the impact of the size of the air gap on the edge states. The spectrum of the supercell with $g = 0.07a$ is shown in Fig. 11(a), from which one can see that the edge states at $g = 0$ in Fig. 10(a) are brought down in frequency as the confinement effect of the air gap is weakened. The Wannier centers of the states at different fillings of $f = 40$ and 60 are shown in Fig. 10(b). The results show that at these two fillings, edge-localized polarizations also appear at $v_x = \pm 0.5$ while other states show similar features to the results of their Wannier bands as shown in

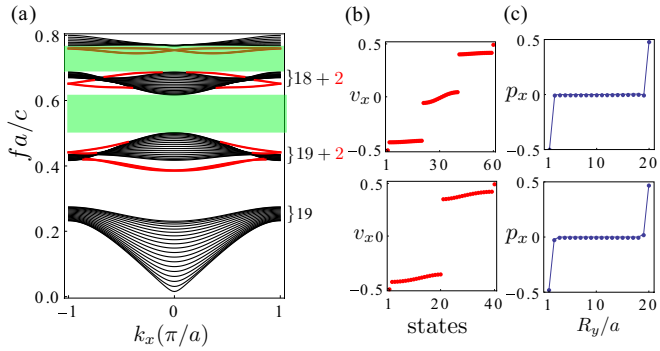

FIG. 11. (a) Projected band diagram of the supercell in Fig. 6(a) with $N_y = 20$ and $g = 0.07a$ at $r = 0.2a$, where the numbers of states for the bulk and edge bands are marked to show the topological properties of the system. The two quadrupole band gaps are shaded as light green. (b) Wannier centers of the bands at different fillings of $f = 40$ and 60. (c) Unit-cell resolved polarization along y at different fillings corresponding to (b).

Figs. 9(a) and 9(c). The unit-cell resolved polarizations along y of the supercell at these two fillings are shown in Fig. 11(c), from which one can see that edge-localized polarizations appear at $R_y = 0$ and $20a$.

The nontrivial bulk quadrupole moments will also result in corner states in a finite system. The spectrum of a finite PhC with size of 10×10 unit cells as shown in Fig. 8(a) as a function of the air gap size is presented in Fig. 12(a), which shows the emergence of two branches of corner states. As the size of the air gap increases, the frequencies of the corner and edge states decrease whereas the frequencies of the bulk states keep unchanged similar to the case of the dipole phases. However, the corner states due to the quadrupole moment are special in

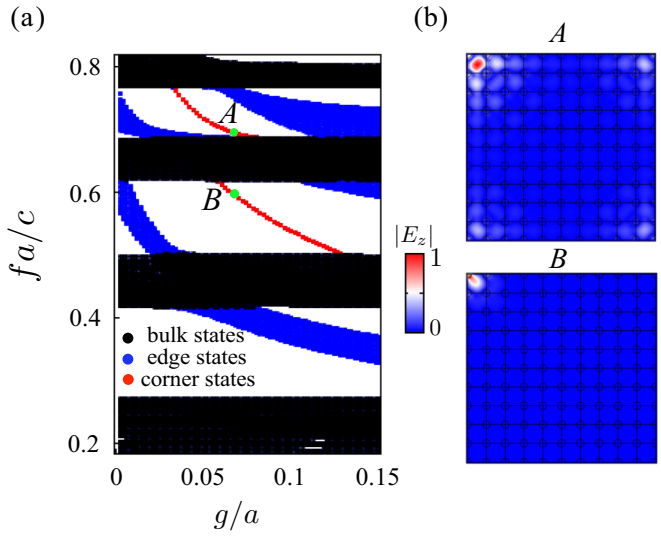

FIG. 12. Spectrum of the system in Fig. 8(a) with $L = 10$ as a function of g at $r = 0.2a$, where the two sets of corner states at $g = 0.07a$ are marked as A and B. The bulk, edge, and corner states are colored as black, blue, and red, respectively. (b) Field profiles ($|E_z|$) of two representative corner states corresponding to the case of A and B, respectively.

that they are located between the two branches of edge states, and have their indices as $100n - 1$, $100n$, $100n + 1$, $100n + 2$ with $n = 2, 3$ for the second and third band gap, i.e., two corner states are coming from the states below the filling of $f = 100n$ and two corner states are from the states above, signaling their nontrivial topological origin. This special distribution of the corner states in the spectrum is the main underlying mechanism for the filling anomaly of the quadrupole corner states to be discussed later. Most strikingly, our system can support two sets of quadrupole corner states within the second and third band gaps simultaneously at $g = 0.07a$ as marked by A and B in Fig. 12(a). The field profiles of one representative corner state from each of the A and B sets are presented in Fig. 12(b), which show that the field distributions of the two branches of red colored states are indeed localized around the system corners, demonstrating their nature as corner states.

The corner states induced by the quadrupole moment could show filling anomaly [21,26]. Our system provides a more interesting scenario as it hosts two sets of corner states and thus allows the study of their interplay at different fillings. Here we study the filling of the two sets of corner states and reveal the signature of their interaction within different band gaps. The average density distributions at different fillings around the corner states within the second band gap, i.e., B as marked in Fig. 12(a), are shown in Figs. 13(a)–13(c) for $f = 198, 200,$ and 202. Note to break the symmetry of the two diagonals, in the simulations, we add a small perturbation in the dielectric distribution. At filling of $f = 198$, due to the lacking of two states, the density distribution shows a corner charge of $Q = -\frac{1}{2}$. At $f = 200$, the density distribution exhibits the typical configuration of a quadrupole, i.e., two positive charges of $Q = \frac{1}{2}$ locate along one diagonal whereas two negative charges of $Q = -\frac{1}{2}$ locate at the other. At filling of $f = 202$, as there are two extra states than neutrality, the four corners now all have corner charge of $Q = \frac{1}{2}$. Interestingly, the existence of the first set of corner states can have a noticeable impact on the filling of the second set of corner states, which is truly remarkable and has not been observed previously. Figures 13(d)–13(f) show the average density distributions at $f = 298, 300,$ and 302. At the filling of $f = 298$, which is different from that at $f = 198$ shown in Fig. 13(a), one can see the small peaks around the corners due to the peaks in Fig. 13(c). At filling $f = 300$, the effect of the first set of corner states can still be seen, modifying the typical feature of density distribution for a quadrupole system. At the filling of $f = 302$, the average density distribution shows similar feature as that of $f = 202$ in Fig. 13(c). To demonstrate that the four small peaks in Fig. 13(d) are indeed caused by the first set of corner states, we show in Figs. 13(g)–13(i) the average density distributions when filling the second set of corner states but without the first set of corner states. In Fig. 13(g), due to the missing of 6 states, the corner charge now shows $Q = -\frac{3}{2}$. In Fig. 13(h), as two additional states are filled, i.e., four are still missing due to the artificially removing of the four corner states in the second band gap, the corner charges now show $Q = -\frac{3}{2}$ and $-\frac{1}{2}$. Finally in Fig. 13(i), when all the four corner states in the third band gap are filled (but two states in total are still missing due to the absence of the first set of corner states), the corner charge now shows $Q = -\frac{1}{2}$. In Figs. 13(g)–13(i), the corner charges exhibit a

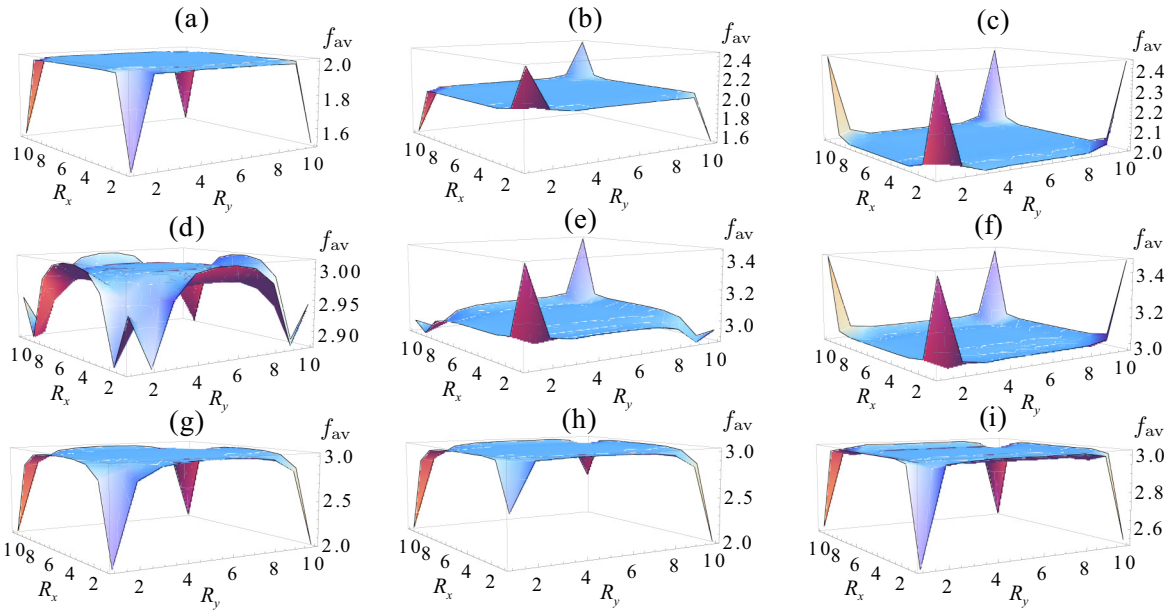

FIG. 13. Filling anomaly of the two sets of corner states marked as A and B in Fig. 12. (a)–(c) Average density distributions at different fillings of $f = 198, 200$, and 202 around the corner states in the first quadrupole band gap. (d)–(f) Average density distributions at different fillings of $f = 298, 300$, and 302 around the corner states in the second quadrupole band gap. (g)–(i) Average density distributions at different fillings of $f = 298, 300$, and 302 in the second quadrupole band gap without considering the corner states in the first quadrupole band gap.

regular distribution rather than the cases with small peaks, which clearly demonstrates that the existence of the first set of corner states can have a nontrivial effect on the filling of another set of corner states located in a different band gap, even though the two sets of corner states are separated by extensive bulk and edge states.

VII. CONCLUSION AND OUTLOOK

In conclusion, we have studied in detail the topological phases of a simple magneto-optical PhC in a square lattice and found that the system can host rich topological physics when choosing the unit cell in such a way that the gyromagnetic cylinders are located at the four corners of the square unit cell. We have used the Wilson loop and nested Wilson loop methods to characterize the topological properties of the different phases, such as Chern, dipole, and quadrupole phases. The nontrivial bulk dipole and quadrupole moments lead to counting mismatch in the bulk bands of systems with open edges, where the missing states appear as edge and corner states within the band gaps. Interestingly, the different topological phases show dual-band property, which provides a convenient setup for investigating the evolution and interaction of the edge and corner states within different band gaps. Our results reveal that these edge and corner states exhibit the striking feature of spectrum robustness. For example, the edge and corner states in the dipole phases can be pushed to and imbedded in the bulk states by modulating the boundary conditions. Nonetheless, these edge and corner states could cross the bulk bands and reemerge in a different band gap. For the quadrupole phases, the system can host two separate sets of corner states within different band gaps and, intriguingly, the filling anomaly of one set of corner states can have impact on the filling anomaly of the other set of corner states, though they are separated by extensive number of bulk states. Our results demonstrate that magneto-optical PhCs can have interesting high-order topological physics, which has been largely overlooked previously.

The tunability of the edge and corner states in the dipole and quadrupole phases by modulating the boundary conditions provides interesting opportunities for practical applications. For example, the possibility of embedding the edge and corner states into the bulk states and releasing them to different band gaps could be harnessed for information storage and transfer in different dimensions (0D, 1D, and 2D). The frequency shifts of the edge and corner states due to changing boundary conditions could be exploited for sensing applications [67,68]. Moreover, the covering of different frequency ranges of the edge states by tuning the size of the air gap is promising for wavelength division multiplexing devices [69–72]. The spectrum robustness implies that the operational bandwidth of the applications is not limited to a single band gap and could be extended to much larger frequency range covered by multiple band gaps.

While in this work we have focused on the first-order Chern phases and second-order dipole and quadrupole phases in the square lattice, many possible extensions could be envisaged. For example, the study of first- and second-order topological phases of magneto-optical PhCs in the hexagonal lattices [73–75] may also lead to new insights. Moreover, in hexagonal lattices, magneto-optical PhCs can have valley or pseudospin polarized states [12,76] due to the breaking of the time-reversal symmetry and, recently, the study of different topological phases in a single setup has attracted a lot of interest [77–79]. So, the interplay of Chern, valley, pseudospin, dipole, quadrupole phases, etc., in a single setup would bring

very rich opportunities. Although finding a suitable PhC structure that can support multiple first-order and higher-order topological phases is not a trivial task, the recent developments in inverse design, deep learning, automated discovery, and optimization [80–82] for designing topological photonic structures may provide a solution.

ACKNOWLEDGMENTS

This research was funded by the National Natural Science Foundation of China (Grant No. 12102134), the Natural Science Foundation of Hunan Province (Grant 2022JJ40026), the Research Grants Council of Hong Kong SAR (Grants No. 15200922, No. 15205219, No. 15202820, and No. 15204419).

[1] F. D. M. Haldane and S. Raghu, Possible realization of directional optical waveguides in photonic crystals with broken time-reversal symmetry, Phys. Rev. Lett. **100**, 013904 (2008).
[2] S. Raghu and F. D. M. Haldane, Analogs of quantum-Hall-effect edge states in photonic crystals, Phys. Rev. A **78**, 033834 (2008).
[3] Z. Wang, Y. D. Chong, J. D. Joannopoulos, and M. Soljačić, Reflection-free one-way edge modes in a gyromagnetic photonic crystal, Phys. Rev. Lett. **100**, 013905 (2008).
[4] Z. Wang, Y. Chong, J. D. Joannopoulos, and M. Soljačić, Observation of unidirectional backscattering-immune topological electromagnetic states, Nature (London) **461**, 772 (2009).
[5] Y. Poo, R.-x. Wu, Z. Lin, Y. Yang, and C. T. Chan, Experimental realization of self-guiding unidirectional electromagnetic Edge States, Phys. Rev. Lett. **106**, 093903 (2011).
[6] A. C. Tasolamprou, M. Kafesaki, C. M. Soukoulis, E. N. Economou, and T. Koschny, Chiral topological surface states on a finite square photonic crystal bounded by air, Phys. Rev. Appl. **16**, 044011 (2021).
[7] S. A. Skirlo, L. Lu, and M. Soljačić, Multimode one-way waveguides of large Chern numbers, Phys. Rev. Lett. **113**, 113904 (2014).
[8] S. A. Skirlo, L. Lu, Y. Igarashi, Q. Yan, J. Joannopoulos, and M. Soljačić, Experimental observation of large Chern numbers in photonic crystals, Phys. Rev. Lett. **115**, 253901 (2015).
[9] B. Bahari, A. Ndao, F. Vallini, A. El Amili, Y. Fainman, and B. Kantè, Nonreciprocal lasing in topological cavities of arbitrary geometries, Science **358**, 636 (2017).
[10] P. Zhou, G.-G. Liu, Y. Yang, Y.-H. Hu, S. Ma, H. Xue, Q. Wang, L. Deng, and B. Zhang, Observation of photonic antichiral edge states, Phys. Rev. Lett. **125**, 263603 (2020).
[11] Z. Ji, J. Chen, and Z.-Y. Li, Perspective: Antichiral magnetic topological photonics, J. Appl. Phys. **133**, 140901 (2023).
[12] G.-G. Liu, P. Zhou, Y. Yang, H. Xue, X. Ren, X. Lin, H.-x. Sun, L. Bi, Y. Chong, and B. Zhang, Observation of an unpaired photonic Dirac point, Nat. Commun. **11**, 1873 (2020).
[13] Z. Lan, J. W. You, and N. C. Panoiu, Nonlinear one-way edge-mode interactions for frequency mixing in topological photonic crystals, Phys. Rev. B **101**, 155422 (2020).
[14] M. Wang, R.-Y. Zhang, L. Zhang, D. Wang, Q. Guo, Z.-Q. Zhang, and C. T. Chan, Topological one-way large-area waveguide states in magnetic photonic crystals, Phys. Rev. Lett. **126**, 067401 (2021).
[15] X. Yu, J. Chen, Z.-Y. Li, and W. Liang, Topological large-area one-way transmission in pseudospin-field-dependent waveguides using magneto-optical photonic crystals, Photon. Res. **11**, 1105 (2023).
[16] J. Chen and Z.-Y. Li, Prediction and observation of robust one-way bulk states in a gyromagnetic photonic crystal, Phys. Rev. Lett. **128**, 257401 (2022).
[17] Y. Zhang, Z. Lan, L. Hu, Y. Shu, X. Yuan, P. Guo, X. Peng, W. Chen, and J. Li, Chiral photonic topological states in Penrose quasicrystals, Opt. Lett. **48**, 2229 (2023).
[18] X. Wang, W. Zhao, H. Zhang, S. Elshahat, and C. Lu, Magnetic-optic effect-based topological state: Realization and application, Front. Mater. **8**, 816877 (2022).
[19] J. Chen and Z.-Y. Li, Topological photonic states in gyromagnetic photonic crystals: Physics, properties, and applications, Chin. Phys. B **31**, 114207 (2022).
[20] W. A. Benalcazar, B. A. Bernevig, and T. L. Hughes, Quantized electric multipole insulators, Science **357**, 61 (2017).
[21] W. A. Benalcazar, B. A. Bernevig, and T. L. Hughes, Electric multipole moments, topological multipole moment pumping, and chiral hinge states in crystalline insulators, Phys. Rev. B **96**, 245115 (2017).
[22] S. Mittal, V. V. Orre, G. Zhu, M. A. Gorlach, A. Poddubny, and M. Hafezi, Photonic quadrupole topological phases, Nat. Photon. **13**, 692 (2019).
[23] Y. Chen, Z.-K. Lin, H. Chen, and J.-H. Jiang, Plasmon-polaritonic quadrupole topological insulators, Phys. Rev. B **101**, 041109(R) (2020).
[24] J. Schulz, J. Noh, W. A. Benalcazar, G. Bahl, and G. von Freymann, Photonic quadrupole topological insulator using orbital-induced synthetic flux, Nat. Commun. **13**, 6597 (2022).
[25] X. Zhou, Z.-K. Lin, W. Lu, Y. Lai, B. Hou, and J.-H. Jiang, Twisted quadrupole topological photonic crystals, Laser Photon. Rev. **14**, 2000010 (2020).
[26] L. He, Z. Addison, E. J. Mele, and B. Zhen, Quadrupole topological photonic crystals, Nat. Commun. **11**, 3119 (2020).
[27] P. Zhou, G.-G. Liu, Z. Wang, Y.-H. Hu, S. Li, Q. Xie, Y. Zhang, X. Xi, Z. Gao, L. Deng, and B. Zhang, Realization of a quadrupole topological insulator phase in a gyromagnetic photonic crystal, arXiv:2302.03184.
[28] F. Liu, H.-Y. Deng, and K. Wakabayashi, Helical topological edge states in a quadrupole phase, Phys. Rev. Lett. **122**, 086804 (2019).
[29] B. Xie, G. Su, H.-F. Wang, F. Liu, L. Hu, S.-Y. Yu, P. Zhan, M.-H. Lu, Z. Wang, and Y.-F. Chen, Higher-order quantum spin Hall effect in a photonic crystal, Nat. Commun. **11**, 3768 (2020).
[30] K.-H. O and K.-H. Kim, Hexagonal photonic crystal with nontrivial quadrupole topology, Photon. Nanostruct.: Fundam. Appl. **54**, 101118 (2023).
[31] Z. Lan, Y. Chen, J. Zhu, and Z. Su, Quadrupole topological phases and filling anomaly in all-dielectric Lieb lattice photonic crystals, Opt. Lett. **48**, 5747 (2023).

[32] J. Jin, L. He, J. Lu, E. J. Mele, and B. Zhen, Floquet quadrupole photonic crystals protected by space-time symmetry, Phys. Rev. Lett. **129**, 063902 (2022).
[33] L. Xiong, Y. Zhang, Y. Liu, Y. Zheng, and X. Jiang, Higher-order topological states in photonic Thue-Morse quasicrystals: Quadrupole insulator and the origin of corner states, Phys. Rev. Appl. **18**, 064089 (2022).
[34] B.-Y. Xie, H.-F. Wang, H.-X. Wang, X.-Y. Zhu, J.-H. Jiang, M.-H. Lu, and Y.-F. Chen, Second-order photonic topological insulator with corner states, Phys. Rev. B **98**, 205147 (2018).
[35] X.-D. Chen, W.-M. Deng, F.-L. Shi, F.-L. Zhao, M. Chen, and J.-W. Dong, Direct observation of corner states in second-order topological photonic crystal slabs, Phys. Rev. Lett. **122**, 233902 (2019).
[36] B.-Y. Xie, G.-X. Su, H.-F. Wang, H. Su, X.-P. Shen, P. Zhan, M.-H. Lu, Z.-L. Wang, and Y.-F. Chen, Visualization of higher-order topological insulating phases in two-dimensional dielectric photonic crystals, Phys. Rev. Lett. **122**, 233903 (2019).
[37] Y. Chen, F. Meng, Z. Lan, B. Jia, and X. Huang, Dual-polarization second-order photonic topological insulators, Phys. Rev. Appl. **15**, 034053 (2021).
[38] L. Lei, S. Xiao, W. Liu, Q. Liao, L. He, and T. Yu, Polarization-independent second-order photonic topological corner states, Phys. Rev. Appl. **20**, 024014 (2023).
[39] K.-H. O and K.-H. Kim, Dual band second-order topological corner states in 2D valley-Hall hexagonal photonic crystals, Phys. Status Solidi B **259**, 2100568 (2022).
[40] Y. Chen, Z. Lan, and J. Zhu, Inversely designed second-order photonic topological insulator with multiband corner states, Phys. Rev. Appl. **17**, 054003 (2022).
[41] X. Zhou, J. Wu, and Y. Wu, Topological corner states in non-Hermitian photonic crystals, Opt. Commun. **466**, 125653 (2020).
[42] J. Jiang, B. Yan, Y. Peng, J. Xie, A. Shi, and J. Liu, Multiband topological states in non-Hermitian photonic crystals, Opt. Lett. **47**, 437 (2022).
[43] Y. Ota, F. Liu, R. Katsumi, K. Watanabe, K. Wakabayashi, Y. Arakawa, and S. Iwamoto, Photonic crystal nanocavity based on a topological corner state, Optica **6**, 786 (2019).
[44] X. Xie, W. Zhang, X. He, S. Wu, J. Dang, K. Peng, F. Song, L. Yang, H. Ni, Z. Niu, C. Wang, K. Jin, X. Zhang, and X. Xu, Cavity quantum electrodynamics with second-order topological corner state, Laser Photon. Rev. **14**, 1900425 (2020).
[45] H.-R. Kim, M.-S. Hwang, D. Smirnova, K.-Y. Jeong, Y. Kivshar, and H.-G. Park, Multipolar lasing modes from topological corner states, Nat. Commun. **11**, 5758 (2020).
[46] W. Zhang, X. Xie, H. Hao, J. Dang, S. Xiao, S. Shi, H. Ni, Z. Niu, C. Wang, K. Jin, X. Zhang, and X. Xu, Low-threshold topological nanolasers based on the second-order corner state, Light Sci. Appl. **9**, 109 (2020).
[47] R. Gong, M. Zhang, H. Li, and Z. Lan, Topological photonic crystal fibers based on second-order corner modes, Opt. Lett. **46**, 3849 (2021).
[48] K.-H. O and K.-H. Kim, Topological photonic crystal fiber with near-zero flattened dispersion, Opt. Fiber Technol. **73**, 103054 (2022).
[49] S. Elshahat, C. Wang, H. Zhang, and C. Lu, Perspective on the topological rainbow, Appl. Phys. Lett. **119**, 230505 (2021).
[50] L. Liang, X. Zhou, J.-H. Hu, H.-X. Wang, J.-H. Jiang, and B. Hou, Rainbow trapping based on higher-order topological corner modes, Opt. Lett. **47**, 1454 (2022).
[51] Y. Chen, Z. Lan, J. Li, and J. Zhu, Topologically protected second harmonic generation via doubly resonant high-order photonic modes, Phys. Rev. B **104**, 155421 (2021).
[52] K.-K. Om and K.-H. Kim, Second-harmonic generation based on the dual-band second-order topological corner states, Phys. Rapid Res. Lett. **16**, 2100427 (2022).
[53] A. Shi, B. Yan, R. Ge, J. Xie, Y. Peng, H. Li, W. E. I. Sha, and J. Liu, Coupled cavity-waveguide based on topological corner state and edge state, Opt. Lett. **46**, 1089 (2021).
[54] Y.-F. Gao, Y.-H. He, A. Maimaiti, M.-C. Jin, Y. He, and X.-F. Qi, Manipulation of coupling between topological edge state and corner state in photonic crystals, Opt. Laser Technol. **155**, 108387 (2022).
[55] Y. Wang, J. Ren, W. Zhang, L. He, and X. Zhang, Topologically protected strong coupling and entanglement between distant quantum emitters, Phys. Rev. Appl. **14**, 054007 (2020).
[56] C. Li, M. Li, L. Yan, S. Ye, X. Hu, Q. Gong, and Y. Li, Higher-order topological biphoton corner states in two-dimensional photonic lattices, Phys. Rev. Res. **4**, 023049 (2022).
[57] M. Kim, Z. Jacob, and J. Rho, Recent advances in 2D, 3D and higher-order topological photonics, Light Sci. Appl. **9**, 130 (2020).
[58] B. Xie, H.-X. Wang, X. Zhang, P. Zhan, J.-H. Jiang, M. Lu, and Y. Chen, Higher-order band topology, Nat. Rev. Phys. **3**, 520 (2021).
[59] Z. Lan, M. L. N. Chen, F. Gao, S. Zhang, and W. E. I. Sha, A brief review of topological photonics in one, two, and three dimensions, Rev. Phys. **9**, 100076 (2022).
[60] Y. Chen, Z. Lan, and J. Zhu, Second-order topological phases in C_{4v}-symmetric photonic crystals beyond the two-dimensional Su-Schrieffer-Heeger model, Nanophotonics **11**, 1345 (2022).
[61] S. Vaidya, A. Ghorashi, T. Christensen, M. C. Rechtsman, and W. A. Benalcazar, Topological phases of photonic crystals under crystalline symmetries, Phys. Rev. B **108**, 085116 (2023).
[62] H.-X. Wang, G.-Y. Guo, and J.-H. Jiang, Band topology in classical waves: Wilson-loop approach to topological numbers and fragile topology, New J. Phys. **21**, 093029 (2019).
[63] M. Blanco de Paz, C. Devescovi, G. Giedke, J. J. Saenz, M. G. Vergniory, B. Bradlyn, D. Bercioux, and A. G. Etxarri, Tutorial: Computing topological invariants in 2D photonic crystals, Adv. Quantum Technol. **3**, 1900117 (2020).
[64] M. L. N. Chen, L. J. Jiang, S. Zhang, R. Zhao, Z. Lan, and W. E. I. Sha, Comparative study of Hermitian and non-Hermitian topological dielectric photonic crystals, Phys. Rev. A **104**, 033501 (2021).
[65] R. Zhao, G.-D. Xie, M. L. N. Chen, Z. Lan, Z. Huang, and W. E. I. Sha, First-principle calculation of Chern number in gyrotropic photonic crystals, Opt. Express **28**, 4638 (2020).
[66] C. Wang, H. Zhang, H. Yuan, J. Zhong, and C. Lu, Universal numerical calculation method for the Berry curvature and Chern numbers of typical topological photonic crystals, Front. Optoelectron. **13**, 73 (2020).
[67] A. Kumar, M. Gupta, P. Pitchappa, Y. J. Tan, N. Wang, and R. Singh, Topological sensor on a silicon chip, Appl. Phys. Lett. **121**, 011101 (2022).

[68] Y. Sun, Z. Mei, X. Xu, Q. Xie, S. Fan, Z. Qian, and X. Liu, The perspective of topological photonics for on-chip terahertz modulation and sensing, APL Photon. **8**, 110901 (2023).

[69] M. Ouyang, L. Lei, L. He, T. Yu, W. Liu, T. Wang, and Q. Liao, Topological coupling and decoupling of photonic crystal waveguides: Application to topological wavelength demultiplexing, Opt. Laser Technol. **156**, 108476 (2022).

[70] Y. Xu, W. Zhou, K. Chen, and X. Huang, Y-branch wavelength demultiplexer based on topological valley photonic crystals, Opt. Laser Technol. **155**, 108422 (2022).

[71] Y. Ruan, X. Qian, H.-X. Wang, Z.-D. Hu, Y. Yang, J. Wang, X. Shen, and Y. Wang, Applications for wavelength division multiplexers based on topological photonic crystals, Photon. Res. **11**, 569 (2023).

[72] X. Wang, Y. Han, H. Fei, H. Lin, M. Zhang, X. Liu, B. Cao, Y. Yang, Z. Chen, and L. Xiao, Design of wavelength division multiplexing devices based on tunable edge states of valley photonic crystals, Opt. Express **31**, 13933 (2023).

[73] H.-X. Wang, L. Liang, B. Jiang, J. Hu, X. Lu, and J.-H. Jiang, Higher-order topological phases in tunable C_3 symmetric photonic crystals, Photon. Res. **9**, 1854 (2021).

[74] S. Wu, B. Jiang, Y. Liu, and J.-H. Jiang, All-dielectric photonic crystal with unconventional higher-order topology, Photon. Res. **9**, 668 (2021).

[75] Y.-C. Zhou, H.-S. Lai, J.-L. Xie, X.-C. Sun, C. He, and Y.-F. Chen, Magnetic corner states in a two-dimensional gyromagnetic photonic crystal, Phys. Rev. B **107**, 014105 (2023).

[76] Z.-G. Chen, J. Mei, X.-C. Sun, X. Zhang, J. Zhao, and Y. Wu, Multiple topological phase transitions in a gyromagnetic photonic crystal, Phys. Rev. A **95**, 043827 (2017).

[77] M. L. N. Chen, L. J. Jiang, Z. Lan, and W. E. I. Sha, Coexistence of pseudospin- and valley-Hall-like edge states in a photonic crystal with C_{3v} symmetry, Phys. Rev. Res. **2**, 043148 (2020).

[78] G. Wei, Z. Liu, L. Wang, J. Song, and J.-J. Xiao, Coexisting valley and pseudo-spin topological edge states in photonic topological insulators made of distorted Kekulé lattices, Photon. Res. **10**, 999 (2022).

[79] Y. Wang, H.-X. Wang, L. Liang, W. Zhu, L. Fan, Z.-K. Lin, F. Li, X. Zhang, P.-G. Luan, Y. Poo, J.-H. Jiang, and G.-Y. Guo, Hybrid topological photonic crystals, Nat. Commun. **14**, 4457 (2023).

[80] Y. Chen, Z. Lan, Z. Su, and J. Zhu, Inverse design of photonic and phononic topological insulators: a review, Nanophotonics **11**, 4347 (2022).

[81] J. Yun, S. Kim, S. So, M. Kim, and J. Rho, Deep learning for topological photonics, Adv. Phys.: X **7**, 2046156 (2022).

[82] S. Kim, T. Christensen, S. G. Johnson, and M. Soljačić, Automated discovery and optimization of 3D topological photonic crystals, ACS Photonics **10**, 861 (2023).